Energy 294 (2024) 130929

Contents lists available at ScienceDirect

Energy

journal homepage: www.elsevier.com/locate/energy

A comprehensive CFD investigation of tip vortex trajectory in shrouded wind turbines using compressible RANS solver

Paulo A.S.F. Silva [a,b,*], Panagiotis Tsoutsanis [a], Jerson R.P. Vaz [c], Marianela M. Macias [d]

[a] Centre for Computational Engineering Sciences, Cranfield University, Cranfield MK43 0AL, United Kingdom
[b] Federal Institute of Brasília, Brasilia, Brazil
[c] Federal University of Pará - Natural Resources Engineering Program, Av. Augusto Correa, N 1 - Belém, PA, 66075-900, Brazil
[d] Department of Mechanical Engineering and Industrial Design, Faculty of Engineering, Universidad de Cádiz, 11519 Puerto Real, Spain

ARTICLE INFO

Dataset link: https://doi.org/10.17862/cranfield.rd.25341871

Keywords:
Wind turbine
Tip vortex
Wake
CFD
Shroud

ABSTRACT

It is well known that a shroud placed around a wind turbine can increase its power coefficient, but it brings complex mechanisms by which the shroud alters the flow passing through the rotor. Such mechanisms impose numerical challenges, as the shrouded turbines present nonlinear behavior in the wake. This paper deals with a comprehensive analysis of tip vortex trajectory in shrouded wind turbines using Reynolds Averaged Navier–Stokes numerical solutions. The analysis includes aerodynamic performance and vortex characteristics of the whole wind turbine. The Multiple Reference Frame is used on a high-order unstructured compressible solver to study both, isolated and shrouded rotor. The NREL Phase VI Unsteady Aerodynamic Experiment rotor is used as a test case. The accuracy of results for wind speeds between 7 and 25 ms^{-1} is discussed. Overall, good agreement is achieved between the computed pressure distributions and the experimental reference values. At stalled blade, more efforts are needed to improve numerical solutions, especially for integrated load quantities. The vortex structure is examined, showing that shroud impacts tip vortex trajectory by the increase of the axial induced velocity at the rotor plane. This result, demonstrates that the classical Prandtl tip loss is not accurate for shrouded turbine analysis, and modern finite blade functions are needed. The influence of the flow conditions on the tip vortex trajectory, flow separation and shroud interaction are also discussed.

1. Introduction

The transition from fossil fuels to renewable energy sources is a crucial step towards achieving a zero-carbon footprint. Shrouded turbines have emerged as a promising solution to enhance the performance of wind farms and improve the range of working conditions but with increased noise levels [1]. By clustering turbines in regions abundant in wind resources, wind farms can maximize their commercial profitability and streamline maintenance operations. Shrouding horizontal axis micro-wind turbines, particularly in urban environments, has proven effective in increasing power output and enabling turbine rotation at lower wind speeds compared to bare turbines [2]. These advantages result in higher energy production and potential cost reductions [3]. Even though the high costs associated with the large structure of the shroud is a huge drawback in its application, shrouded wind turbines offer potential cost savings compared to conventional wind energy systems due to the increased power generation, extended lifespan, reduced blade fatigue and Less energy output sensitivity to yaw [4].

Numerical predictions play a vital role in understanding wind turbine aerodynamics and optimizing wind farm layouts. Various methods have been employed, ranging from simplified Blade Element Momentum (BEM) model to more complex Computational Fluid Dynamics (CFD) techniques. BEM models enable rapid design and analysis of wind turbine rotors, making them invaluable despite inherent limitations. Hansen et al. [5] coupled CFD and 1D axial momentum theory to demonstrate that the power growth of shrouded turbines is proportional to the increment of mass flow through the turbine blades. Rio Vaz et al. [6] proposed a new BEM, in order to extend it to Diffuser Augmented Wind Turbine (DAWT) analysis. This methodology performs a robust semi-empirical one-dimensional analysis by extending the Glauert's correction to bypass the high values of axial induction factor. Vaz and Wood [7] extended this approach to optimize the blade chord length and twist angle distributions of the shrouded turbine, improving the rotor geometry aerodynamically. Silva et al. [8] proposes a new approach for the designing shrouded turbines by incorporating the effect

* Corresponding author at: Centre for Computational Engineering Sciences, Cranfield University, Cranfield MK43 0AL, United Kingdom.
E-mail addresses: paulo.a.silva@cranfield.ac.uk (P.A.S.F. Silva), panagiotis.tsoutsanis@cranfield.ac.uk (P. Tsoutsanis), jerson@ufpa.br (J.R.P. Vaz), marianela.machuca@uca.es (M.M. Macias).

https://doi.org/10.1016/j.energy.2024.130929
Received 5 October 2023; Received in revised form 29 January 2024; Accepted 4 March 2024
Available online 9 March 2024
0360-5442/© 2024 The Authors. Published by Elsevier Ltd. This is an open access article under the CC BY license (http://creativecommons.org/licenses/by/4.0/).

of the diffuser efficiency into the traditional Blade Element Momentum (BEM) model. This modification allows for the development of new expressions for the axial induction factor and thrust, which are crucial parameters for evaluating the performance of shrouded turbine.The research group of Ohya performed impressive experimental [9] and computational work on both the flanged [10] and lens diffuser [11]. According to these studies, the flange allows a higher pressure drop behind the rotor, which increases the turbine performance as the recirculation grows.

Coupling the BEM method with a CFD solver, incorporating the rotor as body forces, offers a powerful solution for analyzing aerodynamic performance and vortex shed. These hybrid methods, known as actuator disk/line models, are much valuable for determining turbine placement in complex terrains [12]. To improve computational efficiency while maintaining accuracy, Xu et al. [13] developed a simplified hybrid model that incorporates boundary layer correction near the blade using free-wake models. Bontempo et al. [14] carried out CFD simulations of an actuator disk with the shroud and highlighted the desired effect of increased mass flow through the rotor with this coupled analysis. Potsdam [15] used an unstructured Reynolds-averaged Navier–Stokes (RANS) solver with overset and adaptive mesh refinement technique to study NREL Phase VI wind turbine aerodynamics. They pointed out the importance on solving the rotor wake to reach convergence of the rotor performance. Troldbolg et al. [16] compared wake simulations using RANS and Detached Eddy Simulation (DES) with actuator line, disk models, and a full rotor. While RANS solutions were similar for all three rotor representations, the actuator models performed poorly in capturing wake breakdown during DES. Grid refinement also played a crucial role in resolving this phenomenon accurately. Gundling et al. [17] utilized adaptive mesh refinement in DES and Large Eddy Simulations (LES) computations, comparing actuator models coupled with free-vortex models and a full rotor. The full rotor case successfully captured wake instabilities, while the actuator models failed after a certain distance. LES computations by Mo et al. [18] encompassed a wide range of inflow wind speeds, demonstrating vortex breakdown capture through grid refinement in the wake. RANS computations by Carrion et al. [19] on the MEXICO wind turbine indicated that wake resolution does not significantly affect integrated loads, while providing insights into vortex stability, domain periodicity, and velocity profiles. Li et al. [20] compared unsteady RANS and DES overset simulations of the NREL Phase VI turbine, considering collective pitch angle variations. For the reference pitch angle, they RANS and DES showed little difference in the averaged forces and moments computations. Thé et al. [21] provided an in-depth review of turbulence filtering effects in wind turbine simulations. They discuss the main drawbacks of RANS models in capturing the unsteadiness of the flowfield and the high computational cost related to LES. As a result, they recommend the hybrid RANS-LES methods as promising technique for solving the wind turbine aerodynamics.

Computational studies play a crucial role in understanding the physics of shrouded turbines due to the high cost associated with experiments. While the disk actuator has been used to mimic the rotor, it fails to capture important aspects of flow behavior near the blade and in the wake [5]. Takashi et al. [22] conducted LES simulations to investigate blade tip vortexes in two types of wind-lens shrouds: long and compact. They observed that blade tip vortices weaken when interacting with the inner surface of the diffuser due to the influence of strong induced vortex rotation in the opposite direction and the static boundary layer. In the long shroud, the blade tip vortices dissipate before reaching the end of the diffuser, while in the compact shroud, they remain strong until the shroud exit but dissipate shortly after due to interference with vortices flowing out of the diffuser. Saleem and Kim [23] performed RANS simulations to study the influence of tip clearance (ranging from 1 to 5%) on power performance. They found that at high speeds (>20 ms^{-1}), increasing the gap from 1 to 3% improves performance, whereas at moderate speeds (10−20 ms^{-1}), the opposite effect is observed, with larger tip gaps having a more pronounced adverse effect on power. Avallone [24] investigated the impact of tip clearance on two DAWTs, studying far-field noise and flow field using Lattice-Boltzmann Very-Large-Eddy Simulations. Smaller tip gaps were found to promote the breakdown of the rotor tip vortex in smaller structures immediately after the rotor plane and induce earlier flow separation on the suction side of the diffuser. The tip clearance also had a strong effect on far-field noise, with an increase of up to 10 dB in the axial direction downstream of the rotor. Dighe et al. [25] carried out Lattice-Boltzmann Large eddy simulations to study the effect of angled inflow on the aeroacoustic performance of shrouded turbines and found that had a positive impact on power performance but with increased noise levels. Wake vortex interaction between the rotor and shroud has been extensively studied in propellers using unsteady RANS and DES simulations [26], with analyses covering composition, 3-D structure, wake contraction, and vortex evolution. Gong et al. [27] extended the study to different scenarios by varying the number of blades. While the physics of propellers are similar to DAWTs systems, the correlation is not as direct due to the significantly higher rotation speeds in propellers. Aranake et al. [28] investigated the influence of airfoil shape on the power coefficient using a transitional turbulence model. The simulations revealed interesting phenomena, such as strong tip vortex promoting attached flow and preventing stall on the inner surface of the diffuser. Alkhabbaz et al. [29] performed a numerical and experimental work on shrouded turbines and highlighted the importance of positioning the rotor on the shroud and how this affect the aerodynamic performance. Rahmation et al. [30] studied micro turbines experimentally and numerically, they found that by adding the duct the helical structure of tip vortex breaks down at earlier cycles. Ching [31] performed large eddy simulations on a wind turbine under two configurations: ducted and open rotor. Using a sliding mesh technique and a structured mesh high-order solver, they observed that the wake of the ducted turbine contained small flow structures, while the open rotor exhibited a consistent hub vortex and weak tip vortices that dissipated rapidly. Bontempo et al. [32] investigated a three bladed version of the NREL Phase VI shrouded and pointed out the differences on operational design point and flow separation with the new design. For a comprehensive review of both numerical and experimental works on diffuser augmented turbines, refer to [33], which categorizes over 150 articles based on shape, arrangement layout, numerical simulations, and experimental studies. Paz et al. [34] assessed CFD modeling approaches, comparing Multiple Reference frame (MRF) and sliding mesh methods for simulating quadcopter rotors. Both approaches effectively exposed expected thrust trends for ground effect on an isolated rotor. In comparison to the sliding mesh, MRF approach showed 9%–12% lower values in thrust computations. They attributed this deviation due to the increased radial velocity diffusion from the static domain approximation. The sliding mesh simulations also required about 8–9 times more computational time tan MRF. Although deviation on relative position of the blade was also found, they suggest the use of MRF model when computational an temporal resources are limited.

The present work uses a high-order open-source solver [35] with MRF capabilities to gain deeper insights into the complex interplay between the rotor and the shroud. Despite partially smeared unsteady effects, high-order schemes help mitigate inherent MRF limitations like numerical diffusion across the virtual rotor-stator interface, enabling salient wake physics capture. It also shows advantages on avoiding severely small timestep constraints and grid skewness issues that can arise when generating moving meshes. The low computational cost also facilitates its use on industrial applications to study meaningful vortex trends, although it does limit resolution of higher frequency transient phenomena. Prior validations using this solver have demonstrated suitability for characterizing mean power performance, tip vortex trajectory and blade vortex interaction on helicopter flows [36–38]. In this sense, this study is focused on trajectory and performance alteration

rather than higher harmonic loading and unsteadiness. The benchmark case NREL Phase VI is used to study the tip vortex trajectory with and without the shroud. The findings shows that shroud impacts tip vortex trajectory by the increase of the axial induced velocity at the rotor plane. The influence of the flow conditions on the tip vortex trajectory, flow separation and shroud interaction are discussed. Our findings reveal profound aerodynamic impacts from increased shrouding power output and altered, weakened tip vortices.

2. Numerical methodology

The open-source code UCNS3d is used as the CFD solver for the present work [35] that has been previously been successfully applied to several challenging flow problems [39–41]. It solves the compressible RANS equations in integral form absolute velocity formulation. The Navier–Stokes equations are discretized using a cell-centered finite volume approach on an unstructured multi-block grid, which leads to a set of ordinary differential equations in time:

$$\begin{aligned}\frac{d\mathbf{U}_i}{dt} = &-\frac{1}{|V_i|}\sum_{l=1}^{N_f}\sum_{\alpha=1}^{N_{qp}}\mathbf{F}_c^{n,1}(\mathbf{U}(\mathbf{x}_\alpha,t))\omega_\alpha|A_l| \\ &+\frac{1}{|V_i|}\sum_{l=1}^{N_f}\sum_{\alpha=1}^{N_{qp}}\mathbf{F}_v^{n,1}(\mathbf{U}(\mathbf{x}_\alpha,t),\nabla\mathbf{U}(\mathbf{x}_\alpha,t))\omega_\alpha|A_l| + \mathbf{S}_i,\end{aligned} \tag{1}$$

where t is time, $|V_i|$ is volume of the element. $\mathbf{U}_i$ is a volume average of the conserved variable within the control volume of element i. Summation limits, N_f correspond to the number of adjacent faces per element and N_{qp} is the number of quadrature points employed to approximate the surface integrals. $|A_l|$ is the surface area of the corresponding face, and α correspond to the Gaussian points, with coordinate vector $\mathbf{x}_\alpha$ and weights, ω_α, over the adjacent face. The weight and distribution depends on the order of the Gaussian quadrature rule applied. Consequently, higher integration rule enhance the flux approximation. $\mathbf{F_c}$ and $\mathbf{F_v}$ are the convective and viscous flux vectors, respectively, and $\mathbf{S}$ is the volume averaged source term vector due to the inertia forces and the Spalart–Allmaras turbulence model with rotational correction [42].

Using the absolute velocity formulation, Eq. (1), in the rotating reference frame yields:

$$\mathbf{U}=\begin{bmatrix}\rho\\ \rho u\\ \rho v\\ \rho w\\ E\\ \tilde{\nu}\end{bmatrix},\mathbf{F}_\mathbf{c}^x=\begin{bmatrix}\rho u_r\\ \rho u_r u+p\\ \rho u_r v\\ \rho u_r w\\ E u_r+pu\\ u\tilde{\nu}\end{bmatrix},\mathbf{F}_\mathbf{c}^y=\begin{bmatrix}\rho v_r\\ \rho v_r u\\ \rho v_r v+p\\ \rho v_r w\\ E v_r+vp\\ v\tilde{\nu}\end{bmatrix},\mathbf{F}_\mathbf{c}^z=\begin{bmatrix}\rho w_r\\ \rho w_r u\\ \rho w_r v\\ \rho w_r w+p\\ E w_r+wp\\ w\tilde{\nu}\end{bmatrix},$$

$$\mathbf{F}_\mathbf{v}^x=\begin{bmatrix}0\\ \tau_{xx}\\ \tau_{xy}\\ \tau_{xz}\\ \Theta_x\\ \frac{1}{\sigma}(\nu_l+\tilde{\nu})\frac{\partial\tilde{\nu}}{\partial x}\end{bmatrix},\mathbf{F}_\mathbf{v}^y=\begin{bmatrix}0\\ \tau_{xy}\\ \tau_{yy}\\ \tau_{yz}\\ \Theta_y\\ \frac{1}{\sigma}(\nu_l+\tilde{\nu})\frac{\partial\tilde{\nu}}{\partial y}\end{bmatrix},\mathbf{F}_\mathbf{v}^z=\begin{bmatrix}0\\ \tau_{xz}\\ \tau_{yz}\\ \tau_{zz}\\ \Theta_z\\ \frac{1}{\sigma}(\nu_l+\tilde{\nu})\frac{\partial\tilde{\nu}}{\partial z}\end{bmatrix},$$

$$\mathbf{S}=\begin{bmatrix}0\\ \rho\left(\Omega_2 w-\Omega_3 v\right)\\ \rho\left(-\Omega_1 w+\Omega_3 u\right)\\ \rho\left(\Omega_1 v-\Omega_2 u\right)\\ 0\\ C_{b1}\tilde{S}\tilde{\nu}f_{r1}+\frac{1}{\sigma}C_{b2}(\nabla\tilde{\nu})^2-C_{w1}f_w\left(\frac{\tilde{\nu}}{d}\right)^2\end{bmatrix}, \tag{2}$$

where u, v, w are the absolute velocity components in the Cartesian coordinates x, y and z, respectively, ρ is the density, p is the pressure, $\tilde{\nu}$ is the turbulent viscosity. Assuming a calorically perfect gas, the total energy per unit volume is calculated by $E = p/(\gamma-1)+0.5\rho(u^2+v^2+w^2)$, where $\gamma = 1.4$ is the ratio of specific heats for air at normal atmospheric condition. The kinetic laminar viscosity, ν_l, is computed by the Sutherland's law relating the dynamic viscosity to the gas temperature. The viscous stress tensor τ_{ij}, yields

$$\tau_{ij} = (\nu_l+\nu_t)\left(\frac{\partial\mathbf{u}_i}{\partial\mathbf{x}_j}+\frac{\partial\mathbf{u}_j}{\partial\mathbf{x}_i}-\frac{2\partial\mathbf{u}_i}{\partial 3\mathbf{x}_k}\delta_{ij}\right), \tag{3}$$

where ν_t is the eddy viscosity, δ_{ij} is Kronecker delta and the subscripts i, j, k are the Cartesian components of $\mathbf{x} = x, y, z$. The work performed by the viscous stress and heat conduction, Θ_i, can be written:

$$\begin{aligned}\Theta_x &= u\tau_{xx}+v\tau_{xy}+w\tau_{xz}+\left(\frac{\nu}{Pr}+\frac{\nu_t}{Pr_t}\right)\frac{\gamma}{\gamma-1}\frac{\partial T}{\partial x},\\ \Theta_y &= u\tau_{yx}+v\tau_{yy}+w\tau_{yz}+\left(\frac{\nu}{Pr}+\frac{\nu_t}{Pr_t}\right)\frac{\gamma}{\gamma-1}\frac{\partial T}{\partial y},\\ \Theta_z &= u\tau_{zx}+v\tau_{zy}+w\tau_{zz}+\left(\frac{\nu}{Pr}+\frac{\nu_t}{Pr_t}\right)\frac{\gamma}{\gamma-1}\frac{\partial T}{\partial z},\end{aligned} \tag{4}$$

where, Pr is the Prandtl number and Pr_t is the turbulent Prandtl number. The kinematic turbulent viscosity, ν_t is approximated by the SA turbulence model functions ($\tilde{S}$, f_{r1} and f_w) with closure coefficients (C_{b1}, C_{b2} and C_{w1}) as described in [42].

The Monotone Upstream-centered Schemes for Conservation laws (MUSCL) approach developed by Van Leer [43–46] and their extensions [47] is used to provide high-order accuracy in space. The Harten–Lax–van-Leer-Contact (HLLC) solver [48] with the MinMod limiter is used to evaluate the convective fluxes, including the convective part of the turbulence transport equation. The low mach correction is used on the current calculations to improve the accuracy in the wind turbine flow conditions.

The second order implicit backward Euler time integration method is employed to achieve the steady-state solution. The solution advances in pseudo-time using a local Courant Friedrichs Lewy (CFL) number in each control volume. The linearized system of equations is solved using the Block Incomplete Lower–Upper (BILU) factorization which allows an easy parallelization with reduced computational cost. The contribution of the source Jacobian term, $\frac{\partial\mathbf{S}}{\partial\mathbf{U}}$, is added directly on the diagonal component to keep the its dominance [49]. The diagonal elements of the matrix are stored and inverted directly and the off-diagonal ones are calculated at every stage.

The convergence of the results was assessed by monitoring the changes in torque and thrust over time. The simulations were run for a minimum of 5000 iterations, with additional iterations performed as needed to ensure convergence. Convergence was achieved when the relative difference between the torque and thrust values between subsequent iterations are negligible. This approach ensured that the results were stable and reliable.

The Multiple Reference Frame formulation is used to solve the whole computational domain without conformal interfaces. The rotational and inertial zones are defined at the solver level with no requirement of mesh based interface and grid block definition [37,38]. This shows advantage in preserving the stencil through the interface between the frames of reference. The governing equation at each subdomain are computed with respect to its reference frame and the velocities are stored in the absolute frame. This allows a precise computation of the fluxes on non uniform grids [50] and is commonly used on turbomachinery applications.

3. Results

The two-bladed stall-regulated wind turbine NREL Phase VI was tested on the 80′ × 120′ wind tunnel at the NASA Ames Full Scale Aerodynamic Complex. The 5.029 m radius blades were instrumented at five sections with 22 pressure taps and strain gauges to record blade loads and structural responses. The blade has pitch angle of 3 degrees and rotates at 72 RPM with a tip Mach number of 0.1335. Although the turbine is small for large wind-farm commercial application, its size is suitable for renewable urban rooftop power generation. The experimental tests covered a wide range of operational conditions including wind speeds from 5 to 25 m s^{-1} and yaw angles from 0

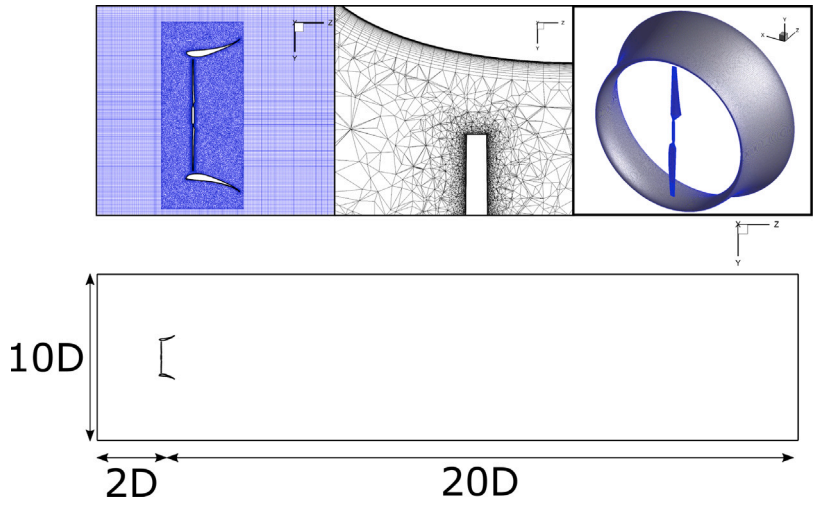


Fig. 1. Schematic of the computational domain (bottom) with details of the mesh refinement around the rotor (top left), tip blade clearance gap (top center) and surface mesh (top right).

to 30°. The large dataset generated by this experiment is a valuable resource for validating numerical codes. Shortly after the experiment was completed, researchers were invited to use their codes to perform a blind study to predict the turbine's performance under the given operating conditions [51]. A variety of methodologies were used on this study, including BEM, free wake and CFD. The predictions were to be widely scattered, even for unstalled flow.

In this work, the computational domain consists in a multi-block hybrid mesh as can be seen in Fig. 1. The guidelines provided by Rezaeiha et al. [52], are followed, with the entire domain consisting of a cylinder of 5.2R of radius and 44R length. The rotor is positioned at 4R and 40R from the inlet and outlet surfaces, respectively, to avoid any spurious influence from the boundary surfaces. The inlet utilizes a turbulence intensity of 0.5% with uniform velocity, representing simplified wind tunnel inflow conditions. No-slip walls are employed for rotor and shroud surfaces. At the outlet surface, characteristic inlet/outlet Riemann boundary conditions is applied, in which the choice of inlet/outlet conditions is made on the extrapolated value of the contravariant velocity at the interface of the boundary. The turbine is represented by a prism block of 21 layers extruded normal to the structured blade surface mesh, with the first layer being at 2×10^{-5} m from the wall with growth rate of 1.2. This wall spacing satisfy the $y^+ < 1$ in compliance with the SA turbulence model and other works in near wall flow separation on this turbine [53].

A grid independence study was conducted by systematically refining the only the blade's surface mesh. Three structured grids were generated with 40, 80, and 160 chordwise nodes. The overall domain used a multi-block topology without wake refinements, resulting in cell counts of 3.85, 6.2, and 15 million. Table 1 summarizes the grid spacing, cell count, torque, thrust, and grid convergence index (GCI) values for the 7 m/s case. The CGI values were calculated based on equations presented in [54]. The fine grid was selected based on reaching a GCI below 1%, indicating a spatially converged solution. Estimated discretization uncertainties were 0.6% on torque and 0.5% on thrust based on fine grid GCI. This blade-only refinement assessment verifies adequate resolution of loads, while avoiding unnecessary cells in the far wake. This mesh studies enable practical resolutions balancing accuracy and computational cost. This discretization errors provide quantification of simulation fidelity for subsequent shrouded turbine analysis.

The shroud geometry and a wake refinement region was added to the selected grid to better resolve the vortex structures. Fig. 1 shows an schematic of computational domain dimensions, surface grid and details of mesh refinement around the rotor and on the gap. The shroud is represented by a prism block of 31 layers extruded normal to the structured blade surface mesh, with the first layer being at 2×10^{-6} m from the wall. The shroud surface has 200 nodes around its airfoil shape with 360 elements distributed radially. The wake refinement is a cylindrical block of 7.3 m of radius with 710 perimeter elements and 800 axial nodes. Table 2 provides the element count for each block, giving total meshes of 55.1 and 47.4 million cells for the shrouded and bare turbines respectively. This wake-focused topology enabled sufficient vortex capture while minimizing unnecessary mesh density. The strategy balanced resolution and cost for practical shrouded turbine simulations.

Even though a number of previous studies have performed simulation of the shrouded turbines, only a few has described in detail its geometry and rotor position. In the present study, the shroud geometry was based on the airfoil Selig S1223 since it has already been studied by other numerical work [28]. This geometry consist of a surface revolution of the airfoil with chord of 1R with angle of attack of 15°. The rotor plane is positioned at 25% of the shroud chord length and the tip clearance gap is set as 0.05R as shows Fig. 2.

3.1. Effect of shroud on aerodynamic forces

Fig. 3 shows the pressure distribution at five radial sections for all inflow conditions. At all five stations, the pressure coefficients (c_p) predictions fairly agree with the experimental data. The computed c_p at the 7 m s^{-1} (red line) matches with the experimental data (□) at all locations. The same stands for the inflow at 10 ms^{-1}, apart from the flat profile over $x/c < 0.5$ at r/R = 0.47. This behavior at this particular location is also seen on other numerical solutions [55]. A comparison between the shrouded turbine (Δ) and bare is shown, it can be seen that the shroud increase the pressure distribution on the blade due to the rise in the mass flow through the rotor plane.

An overview of the rotor thrust and torque for experimental and numerical results for all wind speeds are given in Tables 3 and 4, respectively. The experimental and numerical thrust and power are obtained integrating the pressures measurements along the blade. Overall, the predicted values of thrust are in well agreement with experimental range. The torque computations are under-predicted in all cases, except at low speed (7 ms^{-1}) in which the flow is attached to the blade the computation agrees with the experimental amplitude. Similar results are also found on other compressible solvers [15,55] and differences regarding the compressibility effect at the tip blade has been reported by other works [57]. At post-stall wind speeds, above 10 ms^{-1}, the discrepancies between experimental and numerical are considerable [53].

Table 1
Grid convergence study results for the 7 m/s operating condition.

Grid	Chordwise nodes	Spanwise nodes	Cell count (million)	Torque (N m)	Thrust (N)	GCI_{torque} (%)	GCI_{thrust} (%)
Coarse	40	574	3.85	725	1250	–	–
Medium	80	574	6.2	745	1280	0.9	0.28
Fine	160	923	15.6	750	1290	0.6	0.00

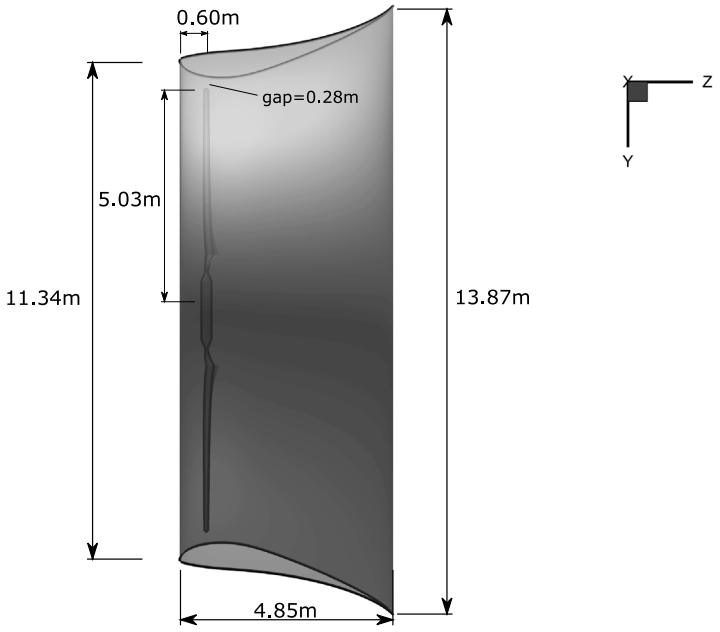


Fig. 2. Dimensions of the shrouded turbine.

Table 2
Mesh information.

Region	Number of elements
Rotor	7.4×10^6
Shroud	2.1×10^6
Wake refinement	21.8×10^6
Off-body shrouded turbine	23.8×10^6
Off-body bare turbine	18.2×10^6

The largest disparity is found at inflow velocity of 15 m s^{-1} which is about 15.2% lower than the minimum experimental value. This occurs because the flow state is critical for the SA-RANS turbulence model as the blade is massively stalled, typically found at low tip-speed ratio condition. Averaged turbulence models are known by their drawback on capturing unsteady flow characteristics. It usually over predicts the attached flow region due to the high production of eddy viscosity on the boundary layer, used to damp the unsteady motion of the fluid. Other works which includes the turbulence transition models and hybrid RANS/LES simulations shows improvement in accuracy [55,58]. Comparing with the bare case, the improvement on integrated loads with the shroud are considerable, especially for the operational wind-speed 7 ms^{-1} which increased about 1.87 and 1.7 times the torque and thrust, respectively. Using similar geometry, Bontempo et al. [32] reached an improvement about 2 times bigger on the shrouded turbine on torque computations while Aranake et al. [28] found an increase of around 1.91 times on thrust predictions. These improved results for torque and thrust are important because the shroud can extend the range of the turbine operating condition, mainly at low wind-speed, as pointed out in [59], which suggest that shrouded wind turbines have much flatter power curves than bare ones. Also, the increase on rotor thrust needs attention, as it can increase drivetrain resistance, since bearing friction depends on the rotor axial load. On the order hand, the torque increases four times compared to the bare rotor, indicating that the shroud can improve turbine starting performance.

3.2. Effect of the shroud on the near wake

Figs. 4 and 5 compare time-averaged q-criterion contours between the bare and shrouded turbines, with vertical lines spaced one rotor diameter apart. In the bare turbine wake, the helical tip and root vortices exhibit persistence over several rotations downstream, preserving coherence. However, the presence of the shroud significantly impacts the tip vortex behavior. Turbulent interactions with the duct boundary layer and wake flow induce early vortex decay, with the tip vortex fading beyond detectability by 8D behind the rotor. At 10 m/s inflow, the initially stronger tip vortex and its faster interaction with the shroud enable marginally greater longevity. However, after diffuser passage, rapid dissipation still occurs due to immersion in the wake turbulence. Other interesting feature is the disruption of the phase relationship between the tip and root vortices by the shroud. At 7 m/s, the vortices appear synchronized between the bare and shrouded cases. But at 10 m/s, the altered tip vortex phase likely contributes to pronounced radial expansion of the root vortex beginning approximately 4D downstream. In summary, the presence of the shroud significantly impacts the persistence, rotational phase synchronicity, and coherence of the helical wake vortex structures.

Isosurface visualization of the q-criterion colored by vorticity magnitude reveals salient differences in wake vortex characteristics between the isolated and shrouded wind turbines, Figs. 6 and 7. In the shrouded case, the helical tip vortex trajectory is evident convecting through the diffuser, enveloped by the wake of the duct itself. While not as destructive as studies utilizing tighter tip clearance gaps have shown [24], this wake turbulence interaction nonetheless rapidly attenuates the tip vortex strength and coherence. Conversely, the isolated turbine maintains a coherent tip vortex structure persisting for several

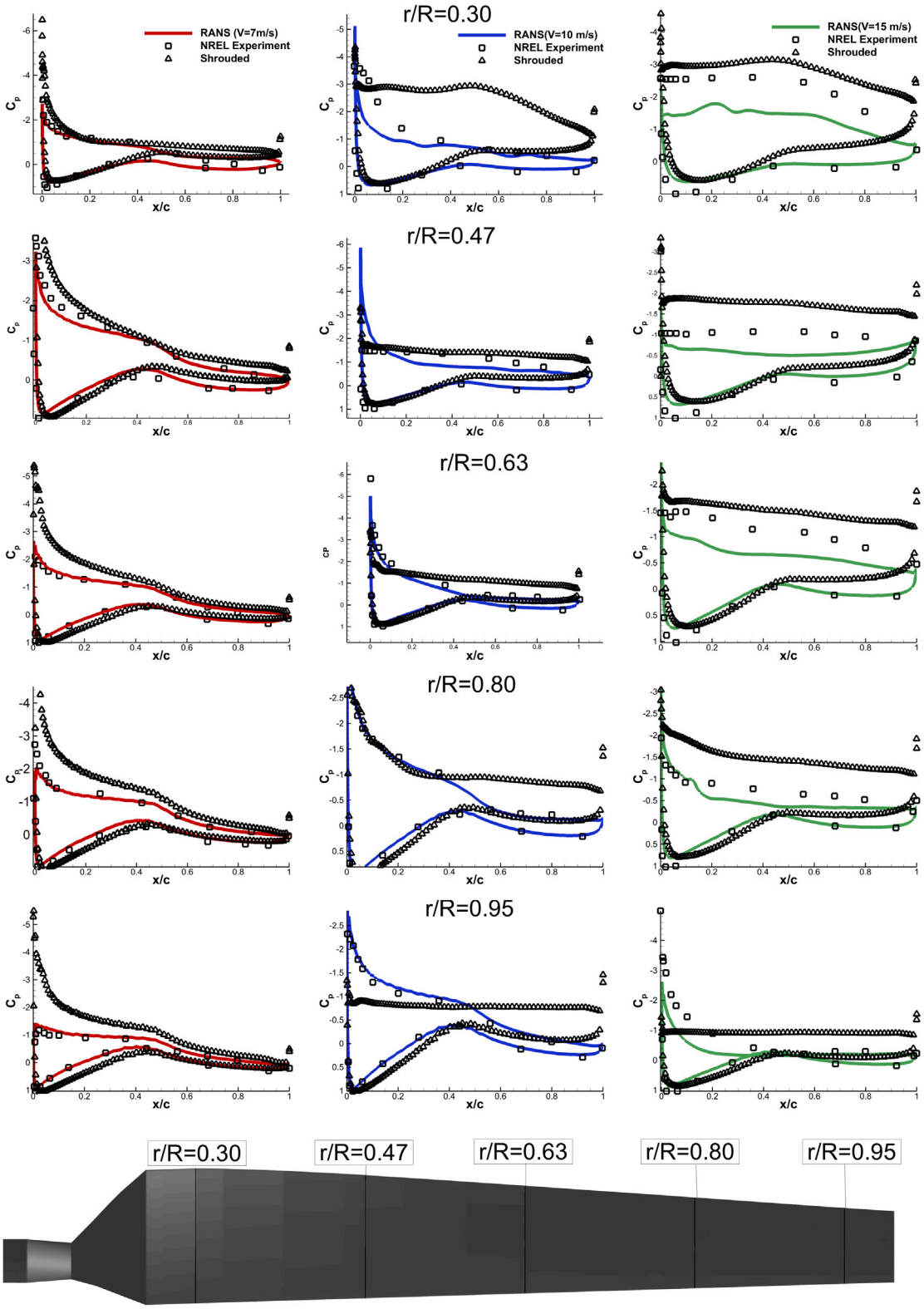


Fig. 3. Numerical and experimental data [56] of pressure coefficient at wind speed ranging from 7 to 15 ms^{-1} for five radial positions: (a) r/R = 0.3, (b) r/R = 0.47 (c) r/R = 0.63 (d) r/R = 0.80 and (d) r/R = 0.95.

rotations downstream. For the shrouded case, dissipation to incoherence occurs within just a few rotational cycles after duct passage. At 10 m/s inflow velocity, Fig. 7, the vortex system persists further downstream, yet remains significantly attenuated by immersion in the diffuser wake. An intriguing divergence is the apparent resilience of the root vortex to shroud effects, maintaining stability across much of the domain.

To analyze the impact of the shroud on tip vortex trajectories, points along the vortices were extracted from q-criterion isosurfaces originating at the blade tips. Fig. 8 provides a planar perspective of

Table 3
Comparison thrust predictions with experimental range.

Velocity [m s^{-1}]	Bare (Shrouded) [N]	Exp. Mean [N]	Exp. max [N]	Exp. min [N]
7	1248.1 (2195.5)	1149	1188	1076
10	1540.9 (2565.8)	1663	1905	1500
15	2058.9 (4098.3)	2278	2754	1383

Table 4
Comparison torque predictions with experimental range.

Velocity [m s^{-1}]	Bare (Shrouded) [N m]	Exp. Mean [N m]	Exp. max [N m]	Exp. min [N m]
7	731.2 (1370.7)	796	822	727
10	1043.9 (1873.7)	1313	1431	1206
15	578.4 (2208.1)	1104	1622	682

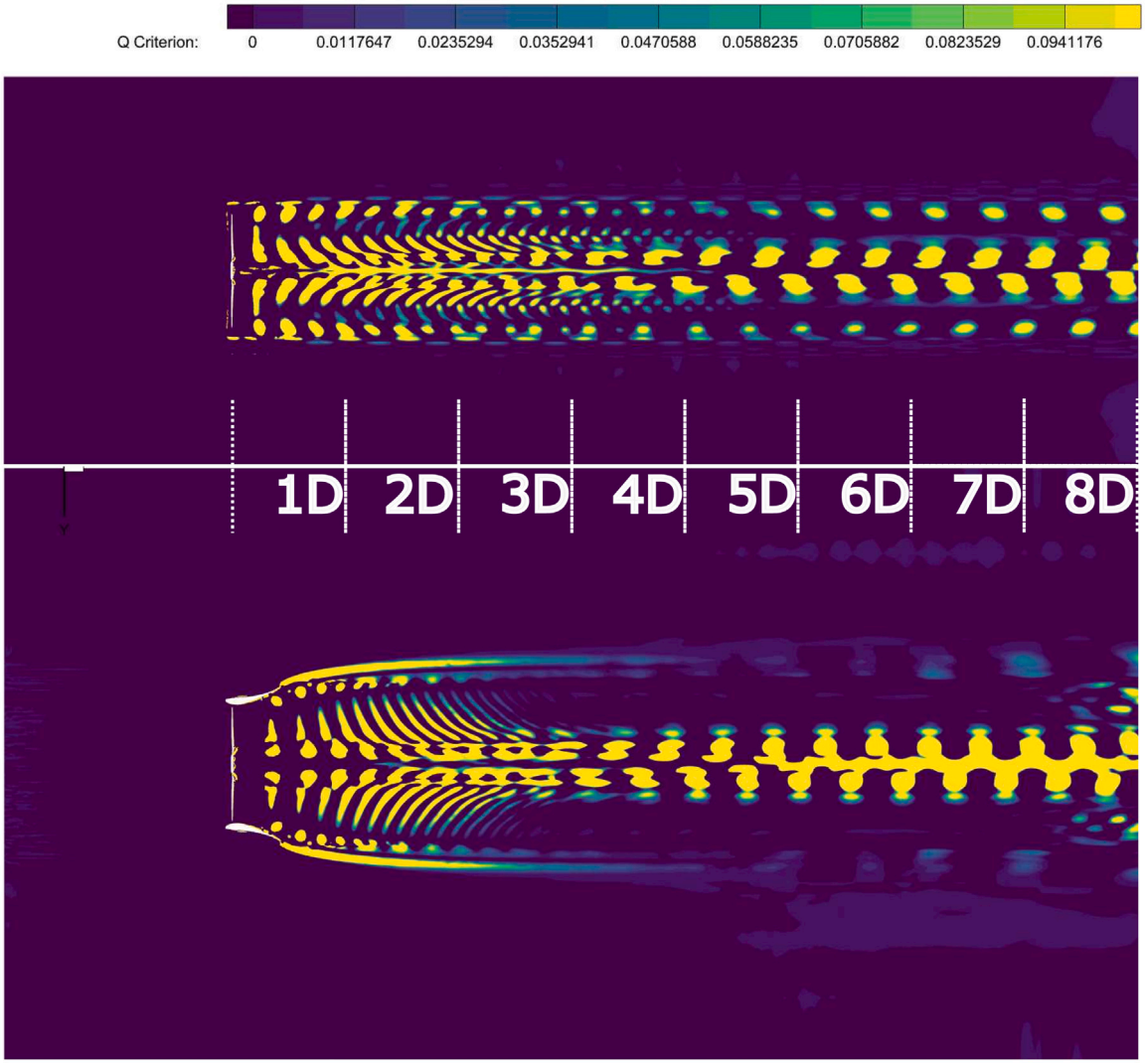


Fig. 4. Contours of q-criteria for the bare turbine (top) and shrouded turbine (bottom) at wind speed equal to 7 ms^{-1}.

the evolving helical paths, unrolling the trajectories over at least 6 rotations downstream. On the bare turbine, the characteristic helical curves are clearly visible. However, on the shrouded turbine, the tip vortex path becomes highly perturbed. At 7 m/s wind speed, the helical structure rapidly destabilizes after passing the rotor, with the radius and rotational frequency varying irregularly. At 10 m/s, the duct still disrupts the trajectory but effects are less pronounced. The primary impact is an accelerated change in vortex rotational rate as it convects downstream. These visualizations reveal that the presence of the shroud significantly alters the tip vortex behavior, inducing unsteady effects and turbulence that disrupt the helical patterns. The faster the vortex moves through the duct, the less weakened it becomes, but its rotational velocity and stability are nonetheless modified compared to the bare case.

Fig. 9 illustrates the development of the tip vortex age in terms of deg and axial direction. On all simulations the bare turbine presents a linear wake age growth rate for most of the data range. This rate slightly varies from one cycle to another as the distance between each

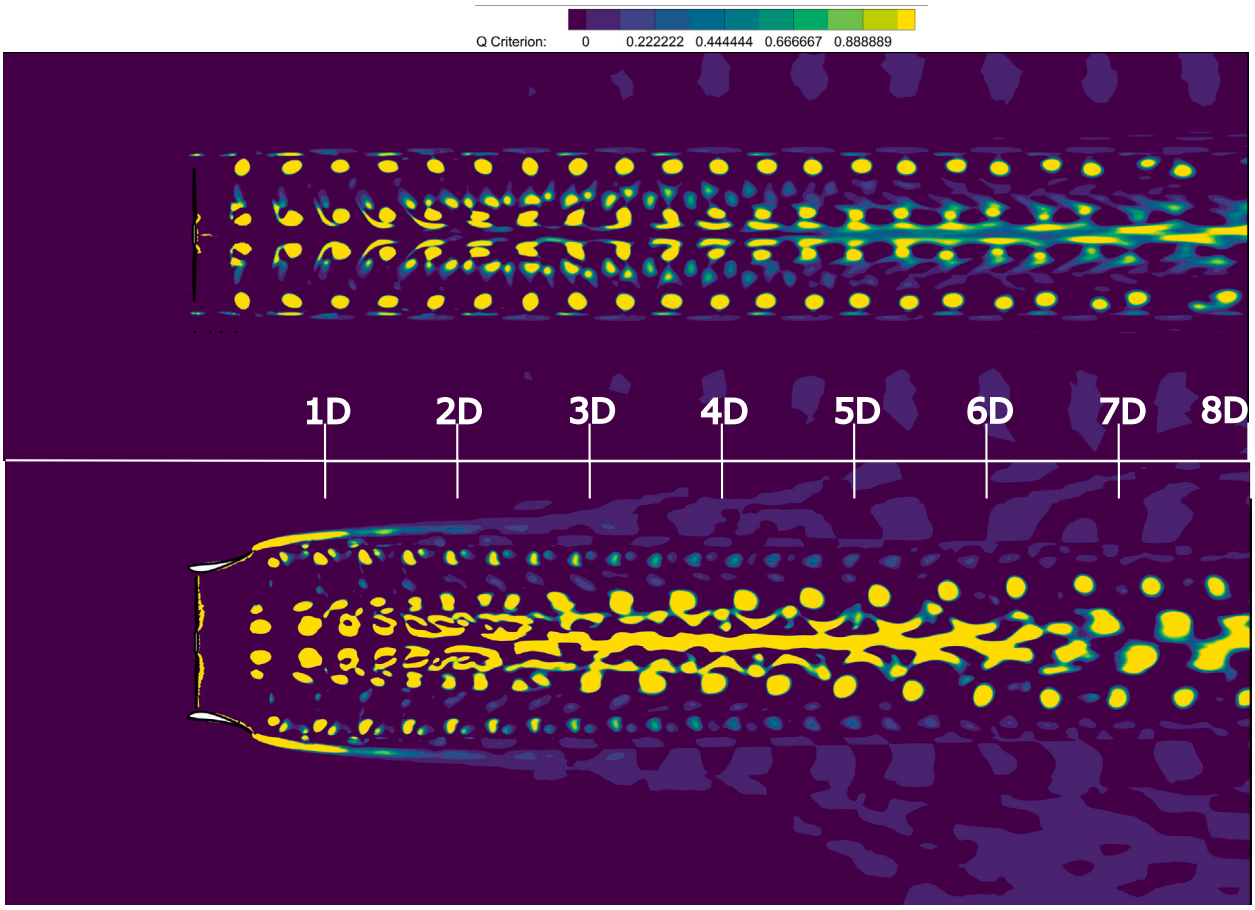


Fig. 5. Contours of q-criteria for the bare turbine (top) and shrouded turbine (bottom) at wind speed equal to 10 ms^{-1}.

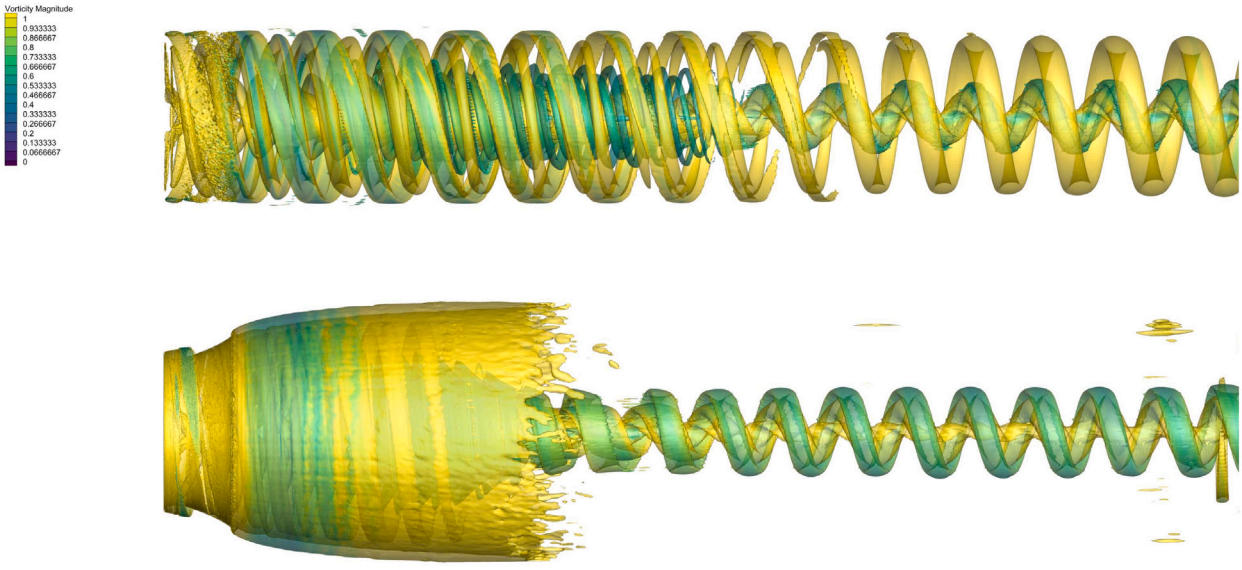


Fig. 6. Comparison of isosurfaces of q-criteria colored by the vorticity magnitude for the bare (top) and shrouded turbine (bottom) at wind speed equal to 7 ms^{-1}.

turn decrease with the axial distance. The influence of the shroud is clearly seen on the first cycle. Even tough a linear trend is seen up to 50 deg, the main helical vortex experiences an exponential distortion for at least the first 300 deg. This nonlinear behavior of the wake for the shrouded turbine demonstrates that finite blade effects cannot be accurately described by models based on wake represented by a two-dimensional set of equally spaced semi-infinite laminae, as it is, for example, by the classical Prandtl's tip loss factor. Prandtl's model is the

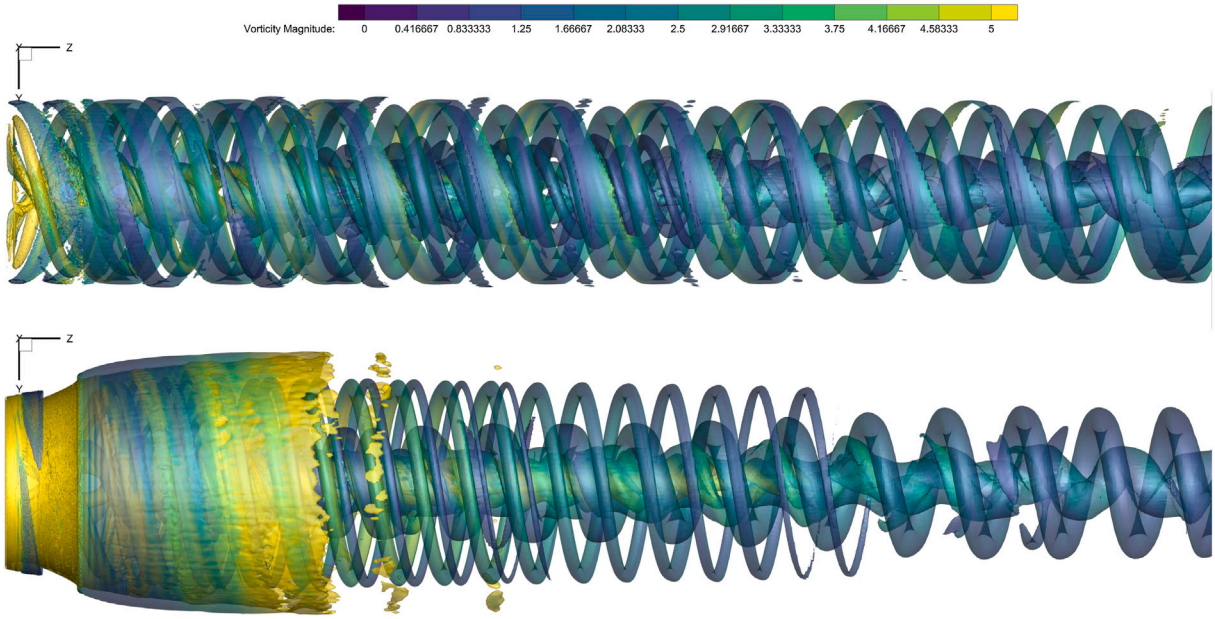


Fig. 7. Comparison of isosurfaces of q-criteria colored by the vorticity magnitude for the bare (top) and shrouded turbine (bottom) at wind speed equal to 10 ms^{-1}.

ratio of the total bound circulation of the blades and the circulation of a rotor with an infinite number of blades. Indeed, Prandtl's factor shows good agreement with free wake vortex theory, but only for bare turbines. As pointed out by [59], alternatives finite blade functions for shrouded rotors are needed, in order to consider the difference between axial and circumferential induced velocities at a shrouded blade. After the first cycle, the shrouded tip vortex shows a linear grown but at a faster rate when compared to the bare case. As a result, the distance between consecutive cycles smoothly decrease as we move downstream the rotor. For all cases presented here, the shroud seems to not affect much the axial distance of the first cycle, but it gradually decrease this gap for the remaining turns. For instance, for the axial range illustrated we can see that the bare turbine experiences 5 cycles while the shrouded 7 cycles, even tough they reach the first 360 deg at similar downstream position. For higher wind speed, this effect is damped on initial cycles but it becomes noticeable after a few turns.

3.3. Tip-vortex and shroud interaction

Fig. 10 shows q-criteria contours at angular slices for the wind speed equal to 7 ms^{-1}, at each 30°, to illustrate the vortex evolution on the wake with a detailing zoom view on its interaction with the shroud. At 30° the tip vortex passes in a close proximity of the shroud and it can be seen an initial interaction the vorticity shed by the shroud's boundary layer. From 60–210°, the tip vortex passes in proximity to the shroud's inner surface and promotes a single laminar separation bubble on the boundary layer due to adverse pressure gradient. As it reaches the shroud exit, at 210°, the tip vortex interacts with the wake and satellite vortices shed by the shroud. Overall, the inner shroud surface experiences substantial flow separation and sheds a large, irregular wake due to the passage of the blade tip vortex. This re-energizes the shroud boundary layer and weakens the blade tip vortex. The blade tip vortex and the induced vortex interact with each other as they roll up forming a helical structure.

Other numerical works using LES computations also reported similar vortex system interaction between tip vortex and shroud. Using a commercial software with sliding mesh on a wind-lens shroud, Takeshi et al. [22] also noted this interference of the blade tip vortices by the induced vortex at the shroud boundary layer. Their results also indicates a thinning process shroud boundary layer which is not clearly seen on the present study due to inherent limitations of the RANS modeling. Avallone et al. [24] used Lattice Boltzmann very large eddy simulations to study the influence of the clearance gap on three-bladed shrouded rotor found that while the tip vortex are rolling along the shroud two vortices counter-rotating secondary vortex generates. In their case, for the similar clearance gap (0.025R) case the vortex also does not breakdown and it gets heavily weakened with the shroud interaction and wake expansion due to airfoil curvature. The present results are more comparable to those reported on LES computations by Aranake et al. [28] as we share the shroud design and similar tip clearance. On Aranake et al. [28] work the tip vortex passage through the shroud oscillates the vorticity shed by the wall surface and the boundary layer height. According to them, this interaction helps on preventing the stall on the shroud since the fluid in the boundary layer is decelerated as the tip vortex is going past. This contrast with the present work may be related to turbulence modeling, as Aranake et al. [28] used transitional models and in the present work the boundary layer is computed by the fully turbulent SA model. Deviation may also be introduced with geometry differences such as axial positioning of the rotor in relation to the shroud and tip clearance gap size. Bontempo et al. [32] used analogous shrouded turbine set-up but with a three blade rotor. They also highlighted that Flow separation occurs on the blade suction side near the tip, forming a tip leakage vortex that sheds downstream of the rotor in a helical path.

Fig. 11 shows the pressure coefficient (Cp) distribution along the shroud inner surface for inlet velocities of 7 m/s and 10 m/s. The plots include Cp at various angular locations, with 0 degrees corresponding to the turbine blade position. A pronounced suction peak is observed at this azimuth due to the strong tip vortex interacting with the shroud. As the helical vortex wake convects along the shroud, it creates oscillating perturbations in the Cp distribution that are clearly visible for 7 m/s approaching the shroud trailing edge. At 10 m/s, the faster moving tip vortex produces smaller oscillations concentrated near the diffuser exit. The weakened intensity relates to the vortex rapid dissipation from interaction with the shroud boundary layer and shear layer, as

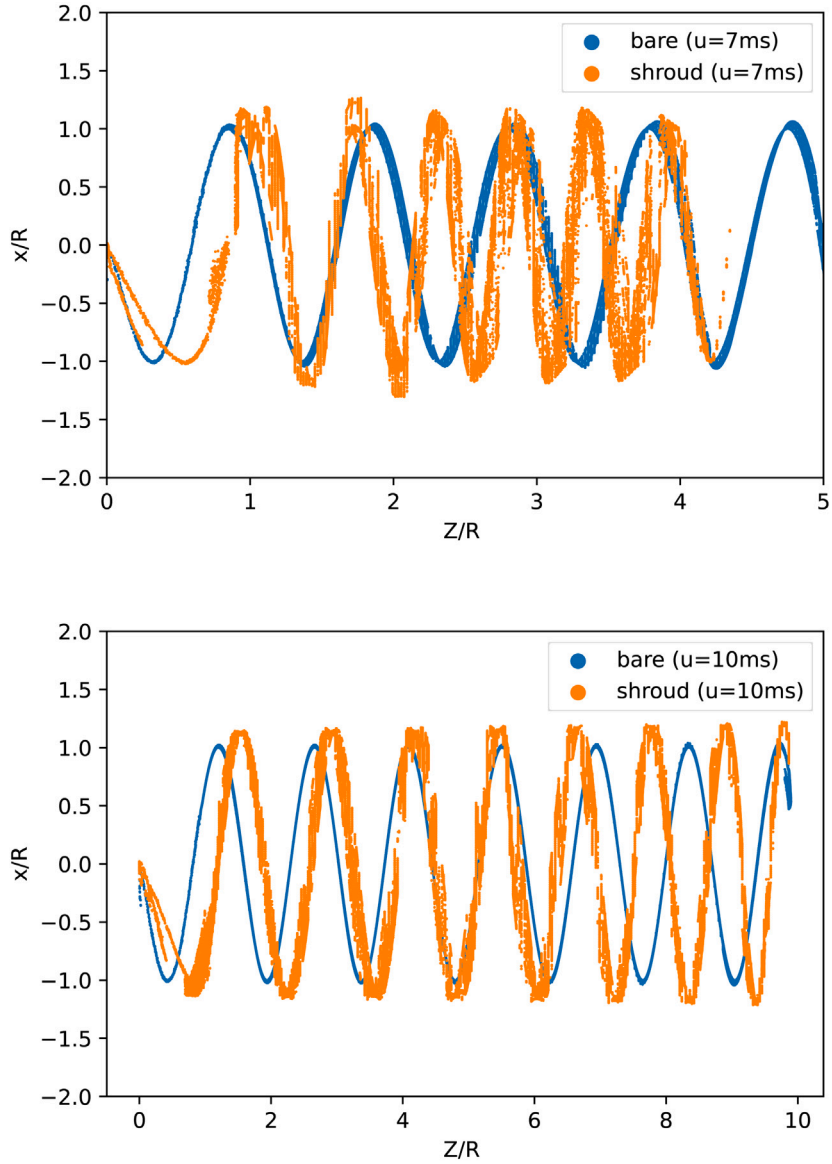


Fig. 8. Planar view of the helical tip vortex development for wind speeds: 7 ms^{-1} (top) and 10 ms^{-1} (bottom).

discussed in previous sections. The pressure maps quantitatively show the footprint of the tip vortex passage along the shroud, inducing periods of elevated suction. The magnitude and extent of the unsteady effects increase with proximity to the rotor plane where vortex strength peaks.

4. Conclusions

In the present paper, the UCNS3D solver was used to simulate the aerodynamic performance of bare and shrouded wind turbines. Numerical solutions obtained by the finite volume, high-order discretization approach by solving 3D compressible RANS equations on mixed-element unstructured grids in a Multiple Reference Frame formulation. The following conclusions are derived from the present study:

- Overall, the compressible Navier–Stokes equations within an Multiple Reference frame formulation has been successfully capable to predict the pressure coefficient at the wide range of radial blade stations and wind speed for high tip-speed ratio condition.
- Concerning the integrated loads on a bare turbine, the predicted values of thrust are in good agreement with experimental range. Torque, on the other hand, is a slightly under predicted in most cases. An increase of 87% in torque for the operational wind speed of 7 m/s is found when the shroud is coupled. This is good to turbines operating at low wind speed.
- On bare turbines, the tip vortex is well preserved and stable for most of computational domain. As it progress on the wake, it experiences a slow radial expansion and linear age growth.
- On shrouded turbines, the tip vortex interacts with the shroud's boundary layer creating adverse pressure gradient of sufficient magnitude to cause the flow to separate, then small laminar separation bubbles is seen on the simulations. This exchange of turbulent energy weakens and destabilize the tip vortex.
- As the shroud increases the axial velocity rather than the circumferential one, its wake helical path change considerable and the distance between tip vortex decreases at faster rate when compared to the bare turbine. This complex behavior demonstrates the need in to consider alternatives for tip loss factor applied to shrouded turbines. The root vortex, on the other hand, remain stable for a few turns before being disturbed by the turbulent flow.

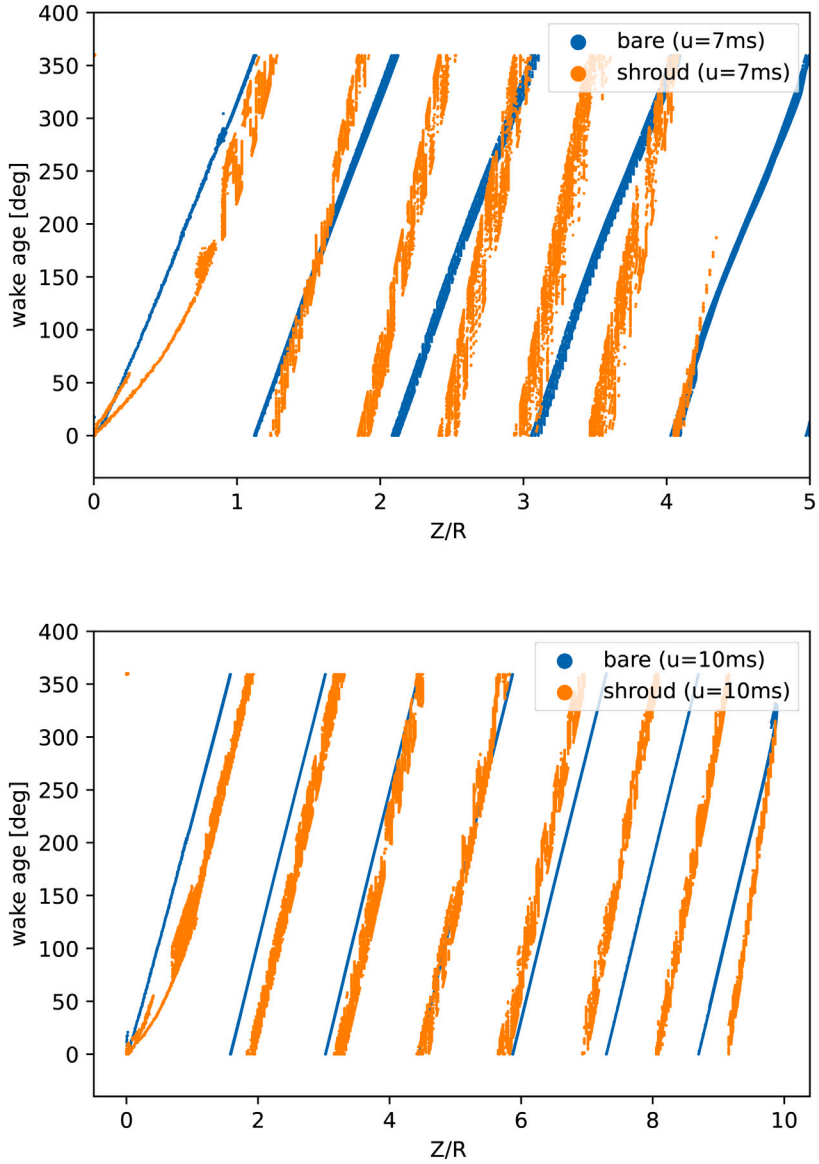


Fig. 9. Tip vortex trajectory in terms of wake age and Z on shrouded and bare turbines for wind speeds: 7 ms^{-1} (top) and 10 ms^{-1} (bottom).

Further work will be conducted to expand the parametric space to optimize key geometric variables such as shroud brim, rotor position, and clearance gaps. Multi-parameter surveys would enable identifying primary performance and tip-vortex sensitivities. Research on the interaction between the helical tip vortex with secondary vortices from shrouds with broad-rings will also expand the understanding of wind turbine wakes. Future work in expanding the MRF approach to wind-farm layouts will enable exploring clustered shrouded turbine interactions with urban near fields and quantifying wake propagation advantages. These advantages will translate to array efficiency gains.

CRediT authorship contribution statement

Paulo A.S.F. Silva: Writing – review & editing, Writing – original draft, Visualization, Validation, Software, Investigation, Conceptualization. **Panagiotis Tsoutsanis:** Software, Resources, Investigation, Funding acquisition. **Jerson R.P. Vaz:** Writing – review & editing, Supervision, Investigation. **Marianela M. Macias:** Writing – review & editing, Writing – original draft, Visualization, Conceptualization.

Declaration of competing interest

The authors declare that they have no known competing financial interests or personal relationships that could have appeared to influence the work reported in this paper.

Data availability

The datasets associated with the test problems presented are available at the Cranfield Online Research Data repository https://doi.org/10.17862/cranfield.rd.25341871.

Acknowledgments

The authors acknowledge the computing time of high-performance computing service Delta of Cranfield University, and ARCHER2 through UK Turbulence Consortium [EPSRC grant number EP/X035484/1]. During this study, Paulo A. S. F. Silva was supported by the Coordenação de Aperfeiçoamento de Pessoal de Nível Superior - Brasil (Capes) - Finance Code 001 (No 88881.707312/2022-01) and Marianela M. Macias by the Margarita Salas grant (NextGenerationEU) from the University of Cádiz.

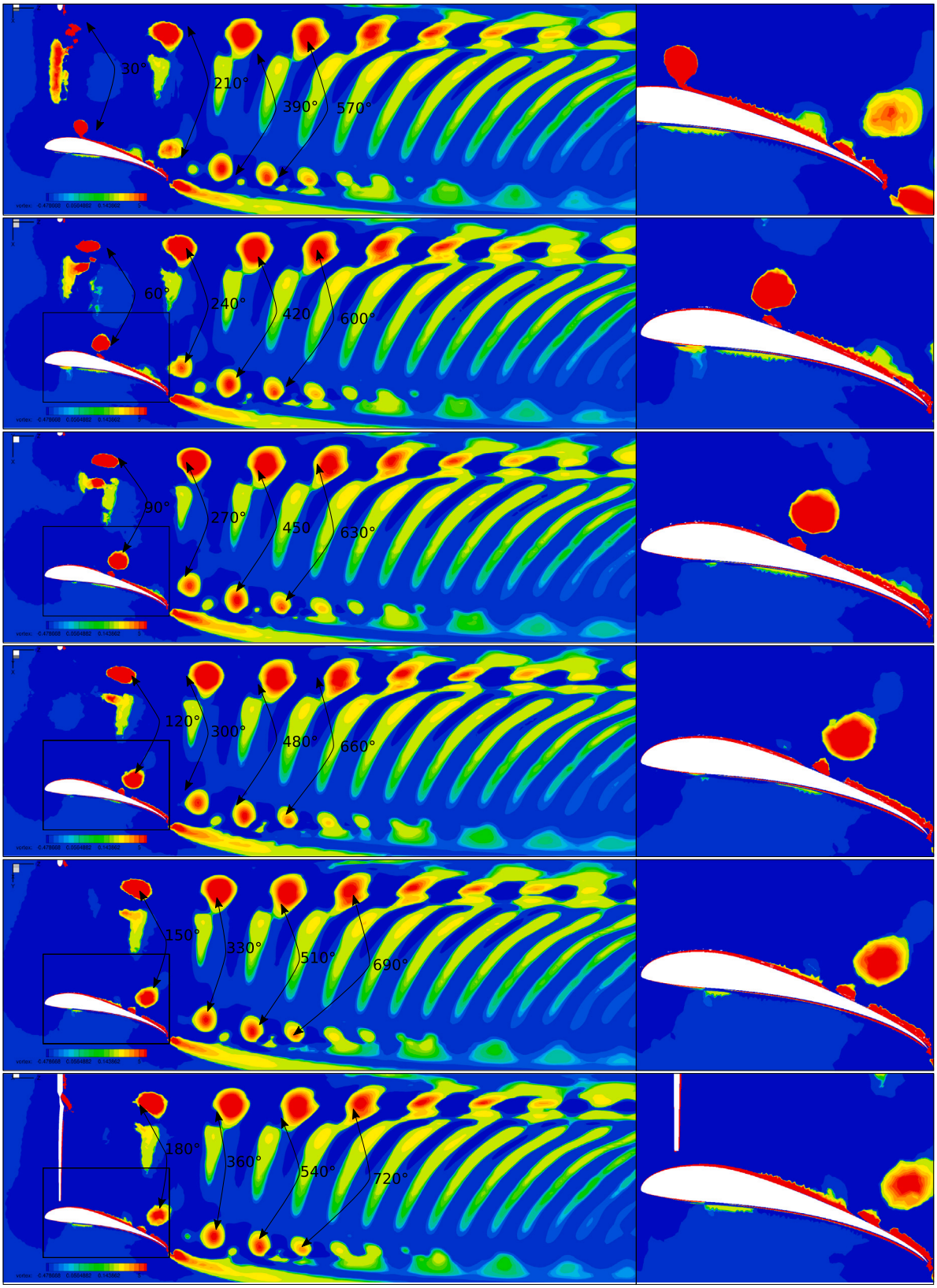


Fig. 10. Contours of q-criteria [s^{-1}] slice of the tip and root vortex age at angular sections at each 30° with shroud vortices interaction in detail.

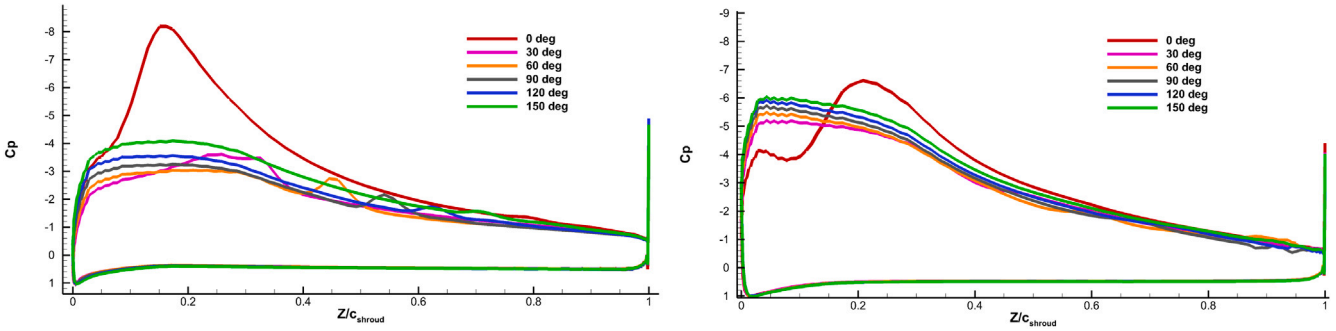


Fig. 11. Pressure coefficient along shroud for several angular slices stations as function of the dimensionless duct-chord coordinate.

References

[1] Hashem I, Mohamed MH, Hafiz AA. Aero-acoustics noise assessment for Wind-Lens turbine. Energy 2017;118:345–68.

[2] Ramos V, Iglesias G. Performance assessment of tidal stream turbines: a parametric approach. Energy Convers Manage 2013;69:49–57.

[3] Vazquez A, Iglesias G. Device interactions in reducing the cost of tidal stream energy. Energy Convers Manage 2015;97:428–38.

[4] Katooli MH, Noorollahi Y. Shrouded wind turbines: a critical review on research and development. Int J Ambient Energy 2022;43(1):8775–91.

[5] Hansen MOL, Sørensen NN, Flay R. Effect of placing a diffuser around a wind turbine. Wind Energy: Int J Prog Appl Wind Power Convers Technol 2000;3(4):207–13.

[6] Rio Vaz DATD, Mesquita ALA, Vaz JRP, Blanco CJC, Pinho JT. An extension of the blade element momentum method applied to diffuser augmented wind turbines. Energy Convers Manage 2014;87:1116–23.

[7] Vaz JR, Wood DH. Aerodynamic optimization of the blades of diffuser-augmented wind turbines. Energy Convers Manage 2016;123:35–45.

[8] Silva PA, Vaz DAR, Britto V, de Oliveira TF, Vaz JR, Junior ACB. A new approach for the design of diffuser-augmented hydro turbines using the blade element momentum. Energy Convers Manage 2018;165:801–14.

[9] Ohya Y, Karasudani T, Sakurai A, Abe K, Inoue M. Development of a shrouded wind turbine with a flanged diffuser. J Wind Eng Ind Aerodyn 2008;96(5):524–39.

[10] Abe K, Ohya Y. An investigation of flow fields around flanged diffusers using CFD. J Wind Eng Ind Aerodyn 2004;92(3):315–30.

[11] Ohya Y, Karasudani T. A shrouded wind turbine generating high output power with wind-lens technology. Energies 2010;3(4):634–49.

[12] Sessarego M, Shen WZ, Van der Laan MP, Hansen KS, Zhu WJ. CFD simulations of flows in a wind farm in complex terrain and comparisons to measurements. Appl Sci 2018;8(5):788.

[13] Xu B, Wang T, Yuan Y, Zhao Z, Liu H. A simplified free vortex wake model of wind turbines for axial steady conditions. Appl Sci 2018;8(6):866.

[14] Bontempo R, Manna M. Performance analysis of open and ducted wind turbines. Appl Energy 2014;136:405–16.

[15] Potsdam MA, Mavriplis DJ. Unstructured mesh CFD aerodynamic analysis of the NREL Phase VI rotor. AIAA paper 1221, 2009, p. 2009.

[16] Troldborg N, Zahle F, Réthoré P-E, Sørensen NN. Comparison of wind turbine wake properties in non-sheared inflow predicted by different computational fluid dynamics rotor models. Wind Energy 2015;18(7):1239–50.

[17] Gundling C, Sitaraman J, Gopalan H, Roget B. A free-vortex wake diffusion model for wind turbines in steady and turbulent atmospheric inflow. In: 51st AIAA aerospace sciences meeting including the new horizons forum and aerospace exposition. 2013, p. 1207.

[18] Mo J-O, Choudhry A, Arjomandi M, Kelso R, Lee Y-H. Effects of wind speed changes on wake instability of a wind turbine in a virtual wind tunnel using large eddy simulation. J Wind Eng Ind Aerodyn 2013;117:38–56.

[19] Carrión M, Woodgate M, Steijl R, Barakos G, Gómez-Iradi S, Munduate X. CFD and aeroelastic analysis of the MEXICO wind turbine. In: Journal of physics: conference series. Vol. 555, 2014, 012006.

[20] Li Y, Paik K-J, Xing T, Carrica PM. Dynamic overset CFD simulations of wind turbine aerodynamics. Renew Energy 2012;37(1):285–98.

[21] Thé J, Yu H. A critical review on the simulations of wind turbine aerodynamics focusing on hybrid RANS-LES methods. Energy 2017;138:257–89.

[22] Takahashi S, Hata Y, Ohya Y, Karasudani T, Uchida T. Behavior of the blade tip vortices of a wind turbine equipped with a brimmed-diffuser shroud. Energies 2012;5(12):5229–42.

[23] Saleem A, Kim M-H. Effect of rotor tip clearance on the aerodynamic performance of an aerofoil-based ducted wind turbine. Energy Convers Manage 2019;201:112186.

[24] Avallone F, Ragni D, Casalino D. On the effect of the tip-clearance ratio on the aeroacoustics of a diffuser-augmented wind turbine. Renew Energy 2020;152:1317–27.

[25] Dighe VV, Avallone F, van Bussel G. Effects of yawed inflow on the aerodynamic and aeroacoustic performance of ducted wind turbines. J Wind Eng Ind Aerodyn 2020;201:104174.

[26] Gong J, Guo C-y, Zhao D-g, Wu T-c, Song K-w. A comparative DES study of wake vortex evolution for ducted and non-ducted propellers. Ocean Eng 2018;160:78–93.

[27] Gong J, Ding J, Wang L. Propeller–duct interaction on the wake dynamics of a ducted propeller. Phys Fluids 2021;33(7):074102.

[28] Aranake AC, Lakshminarayan VK, Duraisamy K. Computational analysis of shrouded wind turbine configurations using a 3-dimensional RANS solver. Renew Energy 2015;75:818–32.

[29] Alkhabbaz A, Yang H-S, Tongphong W, Lee Y-H. Impact of compact diffuser shroud on wind turbine aerodynamic performance: CFD and experimental investigations. Int J Mech Sci 2022;216:106978.

[30] Rahmatian MA, Tari PH, Mojaddam M, Majidi S. Numerical and experimental study of the ducted diffuser effect on improving the aerodynamic performance of a micro horizontal axis wind turbine. Energy 2022;245:123267.

[31] Ding C, Zhang B, Liang C, Visser KD, Yao G. High-order large-eddy simulations of a ducted wind turbine. 2021, arXiv preprint arXiv:2106.00889.

[32] Bontempo R, Di Marzo E, Manna M. Diffuser augmented wind turbines: A critical analysis of the design practice based on the ducting of an existing open rotor. J Wind Eng Ind Aerodyn 2023;238:105428.

[33] Nunes MM, Junior ACB, Oliveira TF. Systematic review of diffuser-augmented horizontal-axis turbines. Renew Sustain Energy Rev 2020;133:110075.

[34] Paz C, Suárez E, Gil C, Vence J. Assessment of the methodology for the CFD simulation of the flight of a quadcopter UAV. J Wind Eng Ind Aerodyn 2021;218:104776.

[35] Antoniadis AF, Drikakis D, Farmakis PS, Fu L, Kokkinakis I, Nogueira X, Silva PA, Skote M, Titarev V, Tsoutsanis P. UCNS3D: An open-source high-order finite-volume unstructured CFD solver. Comput Phys Comm 2022;279:108453. http://dx.doi.org/10.1016/j.cpc.2022.108453.

[36] Ricci F, Silva P, Tsoutsanis P, Antoniadis A. Hovering rotor solutions by high-order methods on unstructured grids. Aerosp Sci Technol 2020;97. http://dx.doi.org/10.1016/j.ast.2019.105648.

[37] Silva P, Tsoutsanis P, Antoniadis A. Simple multiple reference frame for high-order solution of hovering rotors with and without ground effect. Aerosp Sci Technol 2021;111. http://dx.doi.org/10.1016/j.ast.2021.106518.

[38] Silva P, Tsoutsanis P, Antoniadis A. Numerical investigation of full helicopter with and without the ground effect. Aerosp Sci Technol 2022;122. http://dx.doi.org/10.1016/j.ast.2022.107401.

[39] Tsoutsanis P, Dumbser M. Arbitrary high order central non-oscillatory schemes on mixed-element unstructured meshes. Comput & Fluids 2021;225. http://dx.doi.org/10.1016/j.compfluid.2021.104961.

[40] Tsoutsanis P, Adebayo EM, Carriba Merino A, Perez Arjona A, Skote M. CWENO finite-volume interface capturing schemes for multicomponent flows using unstructured meshes. J Sci Comput 2021;89. http://dx.doi.org/10.1007/s10915-021-01673-y.

[41] Antoniadis AF, Tsoutsanis P, Drikakis D. Assessment of high-order finite volume methods on unstructured meshes for RANS solutions of aeronautical configurations. Comput & Fluids 2017;146:86–104. http://dx.doi.org/10.1016/j.compfluid.2017.01.002.

[42] Spalart P, Shur M. On the sensitization of turbulence models to rotation and curvature. Aerosp Sci Technol 1997;1(5):297–302.

[43] van Leer B. Towards the ultimate conservative difference scheme. V. A second-order sequel to Godunov's method. J Comput Phys 1979;32(1):101–36.

[44] Van Leer B. Towards the ultimate conservative difference scheme. IV. A new approach to numerical convection. J Comput Phys 1977;23(3):276–99.

[45] van Leer B. Towards the ultimate conservative difference scheme. II. Monotonicity and conservation combined in a second-order scheme. J Comput Phys 1974;14(4):361–70.
[46] Barth T, Jespersen D. The design and application of upwind schemes on unstructured meshes. In: 27th aerospace sciences meeting. 1989, p. 366.
[47] Tsoutsanis P. Extended bounds limiter for high-order finite-volume schemes on unstructured meshes. J Comput Phys 2018;362:69–94.
[48] Toro EF, Spruce M, Speares W. Restoration of the contact surface in the HLL-Riemann solver. Shock Waves 1994;4(1):25–34.
[49] Yoon S, Chang L, Kwak D. LU-SGS implicit algorithm for three-dimensional incompressible Navier-Stokes equations with source term. In: 9th computational fluid dynamics conference. 1989, p. 1964.
[50] Agarwal R, Deese J. Euler calculations for flowfield of a helicopter rotor in hover. J Aircr 1987;24(4):231–8.
[51] Simms D, Schreck S, Hand M, Fingersh LJ. NREL unsteady aerodynamics experiment in the NASA-Ames wind tunnel: a comparison of predictions to measurements. Tech. rep., Golden, CO (US): National Renewable Energy Lab.; 2001.
[52] Rezaeiha A, Kalkman I, Blocken B. CFD simulation of a vertical axis wind turbine operating at a moderate tip speed ratio: guidelines for minimum domain size and azimuthal increment. Renew Energy 2017;107:373–85.
[53] Lee K, Huque Z, Sui C, Kommalapati R. Prediction of the near wall flow behaviours of separation and transition for NREL phase VI wind turbine blade. Int J Sustain Energy 2023;42(1):545–74.
[54] Celik IB, Ghia U, Roache PJ, Freitas CJ. Procedure for estimation and reporting of uncertainty due to discretization in CFD applications. J. Fluids Eng-Trans ASME 2008;130(7).
[55] Lynch C, Smith M. Unstructured overset incompressible computational fluid dynamics for unsteady wind turbine simulations. Wind Energy 2013;16(7):1033–48.
[56] Hand MM, Simms D, Fingersh L, Jager D, Cotrell J, Schreck S, Larwood S. Unsteady aerodynamics experiment phase VI: wind tunnel test configurations and available data campaigns. Colorado, USA: National Renewable Energy Laboratory Golden; 2001.
[57] Yan C, Archer CL. Assessing compressibility effects on the performance of large horizontal-axis wind turbines. Appl Energy 2018;212:33–45.
[58] Yelmule MM, Vsj EA. CFD predictions of NREL phase VI rotor experiments in NASA/AMES wind tunnel. Int J Renew Energy Res (IJRER) 2013;3(2):261–9.
[59] Vaz JR, Okulov VL, Wood DH. Finite blade functions and blade element optimization for diffuser-augmented wind turbines. Renew Energy 2021;165:812–22.



https://dspace.org/

A comprehensive CFD investigation of tip vortex trajectory in shrouded wind turbines using compressible RANS solver

Silva, Paulo A. S. F.; Tsoutsanis, Panagiotis; Vaz, Jerson R. P.; Macias, Marianela M.

2024-05-01
Elsevier
https://doi.org/10.1016/j.energy.2024.130929
Silva PA, Tsoutsanis P, Vaz JR, Macias MM. (2024) A comprehensive CFD investigation of tip vortex trajectory in shrouded wind turbines using compressible RANS solver. Energy, Volume 294, May 2024, Article number 130929

Downloaded from a DSpace repository. https://dspace.org/